REFERENCE: DY07

NEW DEVELOPMENTS IN VIBRATION REDUCTION WITH ACTIVELY CONTROLLED TRAILING EDGE FLAPS

P.P. Friedmann,[*] T.F. Myrtle,[†] and M. de Terlizzi[‡]
Mechanical and Aerospace Engineering Department
University of California
Los Angeles, California 90095-1597

This paper describes new developments in vibration reduction with actively controlled trailing edge flaps (ACF). This approach is applied to two different problems: (1) vibration reduction at high advance ratios, and (2) alleviation of vibrations due to blade vortex interaction (BVI) at low advance ratios. For the first problem, a new aeroelastic model incorporating trailing edge flaps and a new two-dimensional unsteady aerodynamic theory accounting for compressibility and unsteady freestream effects is used to study three different ACF configurations. For the second problem, BVI at low advance ratios is considered. For this case a different aeroelastic response model was developed by combining a finite element model of the blade, incorporating an actively controlled flap, with a free wake aerodynamic model. It is shown that the two classes of problems have some fundamental differences. Results indicate that the actively controlled flap has remarkable potential for reducing 4/rev vibratory hub shears and moments for both classes of problems.

LIST OF SYMBOLS

a	Lift curve slope
A_R	Rotor disk area
b	Blade semi-chord
c_b	Blade chord
c_{cs}	Control surface chord
C_{do}	Sectional profile drag coefficient
C_h	Sectional hinge moment coefficient
C_f	Flap correction factor
C_l	Sectional lift coefficient
C_m	Sectional moment coefficient
C_W	Weight coefficient, $C_W = \frac{Weight}{\pi L_b{}^2 \rho L_b{}^2 \Omega^2}$
C	Assembled damping matrix
C_n	Rational approximant coefficient matrices
D_0	Generalized flap motion producing constant normal velocity distribution on flap
D_1	Generalized flap motion producing linearly varying normal velocity distribution on flap
EI_y, EI_z	Blade bending stiffnesses in flap and lead-lag, respectively
fC_{df}	Equivalent fuselage flat plate area
f	Vector of generalized forces in the time domain
f_a	Rotor aerodynamic state equations
f_b	Elastic blade equations of motion
f_t	Trim equations
F	Assembled load vector
G	$\mathcal{L}[f(t)U(t)]$
GJ	Blade torsional stiffness
h	Vector of generalized airfoil and flap motions in the time domain
H	$\mathcal{L}[h(t)]$
I	Identity matrix
J	Controller performance index
k	Reduced freq, $\omega b/U$
k_A	Polar radius of gyration of blade cross section, $k_A^2 = (EI_y + EI_z)/EA$
k_m	Mass radius of gyration of blade cross section, $k_m^2 = k_{m1}^2 + k_{m2}^2$
k_{m1}, k_{m2}	Principal mass radii of gyration of the cross section
K	Assembled stiffness matrix
L_b	Blade length
L_{cs}	Control surface length
m	Blade mass per unit length
M	Mach number
M_b	Mass of one blade

[*]Professor
[†]Postdoctoral Scholar
[‡]Research Assistant

M	Assembled mass matrix
n_b	Number of blades
n_L	Number of lag terms
P_{cs}	Average power required to implement the control on a single blade
P_R	Average power required to drive the rotor
q_b	Blade degrees of freedom
q_t	Trim parameters
Q	Matrix transfer function relating generalized motions to aerodynamic loads
$\bar{Q}$	Approximation of Q
s	Laplace variable
$\bar{s}$	Nondim. Laplace variable, $\bar{s} = \frac{sb}{U}$
t	Time
$\bar{t}$	Reduced time, $\bar{t} = \frac{1}{b}\int_0^t U(\tau)d\tau$
T	Matrix of control sensitivities
u	Vector of control input harmonics
Δu	Change in control input harmonics over last time step
U	Freestream velocity
V_F	Helicopter forward flight velocity
W_0	Generalized airfoil motion producing constant normal velocity distribution on chord
W_1	Generalized airfoil motion producing linearly varying normal velocity distribution on chord
W_u	Weighting matrix on control input
$W_{\Delta u}$	Weighting matrix on change in control input
W_z	Weighting matrix on vibration magnitudes
x_{cs}	Distance from blade root to control flap midpoint
x	Aerodynamic state vector for in the time domain, section
x_a	Aerodynamic state vector in the time domain, blade
X_{FA}	Horizontal offset of fuselage aerodynamic center from hub
X_{FC}	Horizontal offset of fuselage center of gravity from hub
X_{Ic}	Offset between hinge point and and the control surface cross-sectional center of mass
z	Vector of 4/rev hub loads.
Z_{FA}	Vertical offset of fuselage aerodynamic center from hub
Z_{FC}	Vertical offset of fuselage center of gravity from hub
α_R	Rotor angle of attack
β	Prandtl Glauert compressibility correction, $\beta = \sqrt{1 - M^2}$
β_p	Blade precone angle
γ_n	Rational approximant pole
γ	Lock Number
δ	Flap deflection angle

ϵ	Dimensionless parameter representative of blade slope
θ_{pt}	Blade pretwist distribution
$\theta_0, \theta_{1c}, \theta_{1s}$	Collective and cyclic pitch components
λ	Inflow ratio
μ	Advance ratio, $\frac{V_F \cos \alpha_R}{\Omega L_b}$
ρ	Air density
σ	Blade solidity ratio
ψ	Blade azimuth angle, $\psi = \Omega t$
$\omega_F, \omega_L, \omega_T$	Rotating flap, lead-lag, and torsional frequencies
Ω	Rotor angular speed
$\dot{(\ )}$	$d(\ )/dt$
$\mathcal{L}[]$	Laplace transform operator

1 INTRODUCTION

Vibration reduction has played a key role in the design of modern helicopters [1,2]. While passive approaches have proven themselves to be effective in the past, new requirements combined with the desire to achieve "jet-smooth" ride in rotary-wing vehicles such as helicopters and tilt-rotors, has motivated the application of active control technology to the rotorcraft vibration problem [3]. The primary advantage of the active control approach consists of the ability to alleviate vibratory loads at their source, before propagating into the fuselage.

There are two distinct classes of vibration problems in forward flight. The first class of problems occurs at high advance ratios where periodic aerodynamic loading of the blades is the primary source of vibratory loads. Active control methods to reduce these loads, at their source, include: higher harmonic control (HHC), individual blade control (IBC), and the actively controlled trailing edge flap (ACF). Recent, as well as current research, has demonstrated that IBC and ACF have considerable advantages over the more dated HHC approach [3]. This class of vibration problems is now reasonably well understood and a number of studies have shown that the actively controlled flap flap retains the most promising aspects of the HHC and IBC approaches while avoiding most of their disadvantages [3].

In the ACF approach, a partial span trailing edge flap is located on the outboard portion of the blade, as shown in Figure 1. This flap is used to dynamically modify the aerodynamic loading along the span. While this vibration reduction process is similar to HHC and conventional IBC, its advantage is that there is no need to oscillate the entire blade or modify the primary control system. Thus, the ACF has the advantage of low power consumption and enhanced airworthiness.

A number of recent studies have confirmed these

expectations. Millott and Friedmann [4] have presented a comprehensive study of the ACF using a fully flexible blade model and modified Theodorsen aerodynamics which include the effect of time-varying freestream. The need for improved aerodynamic modeling was recognized by Milgram and Chopra [6] who have developed an analytical simulation of a helicopter rotor incorporating the ACF using a compressible unsteady aerodynamic model developed by Leishman [7–9]. The aeroelastic model was developed using the comprehensive rotor analysis code UMARC and includes a free wake model with an elastic blade modeled using finite elements. Experimental results from wind tunnel tests of the ACF were also presented in Ref. 5.

Recently, a comprehensive rotor analysis code for the ACF has been developed at UCLA by the authors [10] using a new unsteady aerodynamic model for an airfoil/flap combination based on a rational function approximation (RFA) approach. This aerodynamic model is well suited to rotary wing applications and includes compressibility and unsteady freestream effects. Preliminary results from vibration alleviation studies were presented in Ref. 10 and much more detailed results were presented in Refs. 11 and 12. In addition to vibration reduction, these studies also examine blade stability with a "free-flap" condition as well as a conceptual design for the flap actuation mechanism using piezoelectric materials.

It is also important to mention that very interesting experimental results on the practical implementation of the ACF and its application to fundamental vibration reduction in the open loop mode have been recently reported by Fulton and Ormiston [13].

In a companion study [14] to Refs. 11 and 12, a different problem, namely the BVI alleviation problem at low and moderate advance ratios has been examined, and it was shown that the ACF is also effective in reducing vibrations for this case. The most important finding in Ref.14 was the recognition that vibration reduction at high advance ratios is accomplished using a fundamentally different physical mechanism from that needed for BVI alleviation.

The principal objectives of this paper are to summarize the most important results obtained in Refs. 11 and 14 and present them in a unified and comprehensive framework. The specific objectives of the paper are: (1) description of the two separate aeroelastic models, one used for vibration reduction in high speed flight, and the other used in the BVI alleviation studies, (2) present the vibration reduction studies conducted on three different ACF configurations, namely a servo flap configuration, a plain flap configuration, and a dual servo flap configuration using independent control, (3) present BVI allevia-

tion studies using a servo flap, and (4) demonstrate the fundamental differences between vibration reduction in high speed flight and BVI alleviation using the ACF.

These results presented in this paper make an important contribution toward the implementation of the ACF in a practical setting.

2 AEROELASTIC MODEL FOR HIGH SPEED FLIGHT

The present study is based on an aeroelastic response model for the rotor including the ACF which is described in detail in Refs. 10 and 12, and is also briefly summarized in this section. This model is based on an earlier analysis developed by Millott and Friedmann [4] to study the ACF. The new features of the model consist of an improved aerodynamic model and additional flap configuration options.

2.1 Aerodynamic Modeling

Aerodynamic loads are modeled using a blade element formulation, with sectional loads provided by a new two-dimensional unsteady compressible aerodynamic model [10] recently developed by the authors for an airfoil/flap combination that includes unsteady freestream effects.

The aerodynamic model was developed using a rational function approximation (RFA) [15–17] approach based on the least squares, or Roger's approximation [15]. In this approach, oscillatory aerodynamic response data is used to generate approximate transfer functions that relate generalized motions to aerodynamic loads in the frequency domain.

Consider an aerodynamic system which is represented in the Laplace domain by the expression

$$G(\bar{s}) = Q(\bar{s})H(\bar{s}), \qquad (1)$$

where $G(\bar{s})$ and $H(\bar{s})$ represent Laplace transforms of the generalized aerodynamic load and generalized motion vectors, respectively. Using the Least Squares approach, $Q(\bar{s})$ can be approximated using a rational expression of the form

$$\tilde{Q}(\bar{s}) = C_0 + C_1\bar{s} + \sum_{n=1}^{n_L} \frac{\bar{s}}{\bar{s} + \gamma_n} C_{n+1}. \qquad (2)$$

By using rational expressions, the approximations can be easily transformed to the time domain to yield a state space model for the aerodynamic loads that is compatible with the structural equations of motion and commonly applied control approaches.

In general, the accuracy of the approximation in Eq. (2) depends upon the number of lag terms that

are used. However, each lag term produces a set of aerodynamic states in the time domain which contribute to the 'aerodynamic dimension' of the model. Thus, for computational efficiency, the number of lag terms must be kept to a minimum.

In the present research, a two-dimensional doublet lattice method [18] based on the Possio integral equation [19] is used to generate the necessary compressible flow oscillatory response quantities for a set of generalized airfoil and flap motions over range of reduced frequencies. In addition, the values of the poles γ_n have been optimized to produce a minimum error approximation.

To extend the RFA approach to time-varying freestream, a set of generalized airfoil and flap motions designated W_0, W_1, D_0, and D_1 were chosen which correspond to the normal velocity distributions shown in Figure 2. Using these motions, the model was developed in terms of a reduced time $\bar{t}$, given by

$$\bar{t} = \frac{1}{b} \int_0^t U(\tau) d\tau, \qquad (3)$$

which is proportional to distance traveled. The importance of this transformation has been observed previously in Refs. 20 and 21.

To obtain the time domain expressions, Eq. (2) is first restated in matrix form as

$$\tilde{Q}(\bar{s}) = C_0 + C_1 \bar{s} + D (I\bar{s} - R)^{-1} E\bar{s}, \qquad (4)$$

where

$$D = \begin{bmatrix} I & I & \cdots & I \end{bmatrix}, \qquad (5)$$

$$R = - \begin{bmatrix} \gamma_1 I & & & \\ & \gamma_2 I & & \\ & & \cdots & \\ & & & \gamma_{n_L} I \end{bmatrix}, \qquad (6)$$

$$E = \begin{bmatrix} C_2 \\ C_3 \\ \vdots \\ C_{n_L+1} \end{bmatrix}. \qquad (7)$$

After defining the generalized motion vector $h(t)$ and generalized force vector $f(t)$ as

$$h(t) = \begin{bmatrix} W_0(t) \\ W_1(t) \\ D_0(t) \\ D_1(t) \end{bmatrix}, \quad f(t) = \begin{bmatrix} C_l(t) \\ C_m(t) \\ C_h(t) \end{bmatrix}, \qquad (8)$$

the aerodynamic system in Eq.(1) can be approximated and transformed to the time domain to produce a state space aerodynamic model given by the expressions

$$\dot{x}(t) = \frac{U(t)}{b} R x(t) + E \dot{h}(t), \qquad (9)$$

$$f(t) = \frac{1}{U(t)} \left(C_0 h(t) + C_1 \frac{b}{U(t)} \dot{h}(t) + D x(t) \right). \qquad (10)$$

The aerodynamic loads $f(t)$ are given by Eq. (10), and are a function of a set of aerodynamic states $x(t)$. These states are governed by the set of first order differential equations given in Eq. (9), and are driven by the generalized airfoil and flap motions contained in the vector $h(t)$.

The dimension of the aerodynamic state vector is $n_L \times Num.Forces$. In an aeroelastic simulation, the aerodynamic state equations become coupled with the structural equations of motion and must be solved simultaneously.

To complete the sectional aerodynamic model, aerodynamic drag is given by the sum of profile drag C_{d0} and induced drag using a conventional approach described in Ref. 4. In addition, a multiplicative aerodynamic correction factor C_f is used to scale the aerodynamic loads from flap motion to account for the reduced effectiveness associated with the presence of a gap.

To account for the effect of reverse flow on the aerodynamic loads, lift and moment are set to zero within the reverse flow region, and the drag force is reversed in direction.

2.2 Structural Model

The hingeless rotor blade is modeled as a slender beam composed of a linearly elastic, homogeneous material, cantilevered at the hub as shown in Figure 1. The blade model is taken directly from Ref. 4 and describes the fully coupled flap-lag-torsional dynamics of an isotropic blade. Small strains and finite rotations (moderate deflections) are assumed, and the Bernoulli-Euler hypothesis is used. In addition, strains within the cross-section are neglected. The equations of motion for the elastic blade consist of a set of nonlinear partial differential equations of motion, formulated in the undeformed system, with the distributed loads left in general symbolic form.

The control surfaces are assumed to be an integral part of the blade, attached at a number of spanwise locations using hinges that are rigid in all directions except about the hinge axis, constraining the control surface cross-section to pure rotation in the plane of the blade cross-section (see Fig. 1). The control surface does not provide a structural contribution to the blade, and influences the behavior of the blade only through its contribution to the blade spanwise aero-

dynamic and inertial loading. These structural assumptions apply to all of the flap configurations considered.

When simulating vibration control, flap deflections are assumed to be controlled quantities and do not contribute additional degrees of freedom to the aeroelastic system. However, the code has the capability to simulate a "free-flap" condition that one would encounter when the link operating the flap is broken [11,12]

2.3 Aeroelastic Formulation

The present analysis uses an explicit approach [22] to formulate the aeroelastic equations of motion, with the inertial, structural, damping, and aerodynamic terms appearing as explicit functions of the blade degrees of freedom and aerodynamic states.

Explicit expressions for the distributed inertial, gravitational, and damping loads were derived in Ref. 4 using MACSYMA [23], and have been used in the present analysis. To keep these expressions of manageable size, an ordering scheme [24,25] was used based on a dimensionless parameter ϵ $(0.1 < \epsilon < 0.2)$, which represents typical blade slopes due to elastic deformation. The ordering scheme implies that

$$1 + O(\epsilon^2) \approx 1, \qquad (11)$$

so that terms of order $O(\epsilon^2)$ are neglected in comparison with unity.

In the present study, airloads are not modeled on the inner 20% of the blade span. This assumption is consistent with the design of the MBB BO-105 helicopter blade which is purely structural in this region and does not have an aerodynamic surface.

2.4 Method of Solution

The solution of the rotary-wing aeroelastic response problem is carried out in two steps. First, spatial discretization based on Galerkin's method [24] is used to eliminate the spatial dependence, and subsequently the combined structural and aerodynamic state equations are solved in the time domain.

In this study, Galerkin's method is based on three flap, two lead-lag, and two torsional free vibration modes of a rotating beam. The free vibration modes were calculated using the first nine exact nonrotating modes of a uniform cantilevered beam. Integrations over the blade span associated with the application of Galerkin's method are carried out using Gaussian quadrature. The integrand is evaluated at a specified number of stations along the span of the blade corresponding to Gaussian points; which are determined by the order of Gaussian quadrature being used. The

number and location of these stations must be carefully combined with the implementation of the RFA aerodynamic model. At each station, the sectional airloads are provided by a specific RFA aerodynamic approximation, each contributing a number of aerodynamic state equations to the final model. These state equations are fully coupled with the blade equations of motion through the blade degrees of freedom and aerodynamic states.

The complete aeroelastic model for the blade and actively controlled flap consists of three sets of equations. The first two sets consist of nonlinear differential equations that describe the structural degrees of freedom and aerodynamic states. The equations of motion for the elastic blade are represented by the expression

$$\mathbf{f_b}(\mathbf{q_b}, \dot{\mathbf{q}}_b, \ddot{\mathbf{q}}_b, \mathbf{x_a}, \mathbf{q_t}; \psi) = 0, \qquad (12)$$

where $\mathbf{q_t}$ represents the trim vector, given by

$$\mathbf{q_t} = \{\lambda, \alpha_R, \theta_0, \theta_{1c}, \theta_{1s}\}^T. \qquad (13)$$

The complete set of aerodynamic state equations are given by

$$\mathbf{f_a}(\mathbf{q_b}, \dot{\mathbf{q}}_b, \ddot{\mathbf{q}}_b, \mathbf{x_a}, \dot{\mathbf{x}}_a, \mathbf{q_t}; \psi) = 0. \qquad (14)$$

A third set of equations represent the propulsive trim condition in which force equilibrium is enforced in the vertical plane, and pitch and roll moments are set equal to zero. This flight condition is schematically illustrated in Fig. 3. These equations that were derived in Ref. 4 and include an inflow equation, can be symbolically represented by the expression

$$\mathbf{f_t}(\mathbf{q_b}, \dot{\mathbf{q}}_b, \ddot{\mathbf{q}}_b, \mathbf{x_a}, \mathbf{q_t}; \psi) = 0. \qquad (15)$$

To obtain the coupled trim/response solution, only the steady state response of the system is considered. In this case, the trim condition can be represented by the implicit nonlinear equations

$$\mathbf{f_t}(\mathbf{q_t}) = 0. \qquad (16)$$

Evaluation of Eqs. (16) requires the steady state hub loads that correspond to the trim parameters $\mathbf{q_t}$. These are obtained by integrating Eqs. (12) and (14) numerically over time, until the response solution has converged to the steady state. The trim solution $\mathbf{q_t}$ is obtained using a simple autopilot type controller described in Ref. 10.

2.5 Power Requirements

To characterize the operational requirements of the flap, it is necessary to calculate instantaneous and average control power levels. The instantaneous power

required to drive a single control surface consists of the product of the instantaneous values of the control hinge moment $M_\delta(\psi)$ and the flap deflection rate $\dot{\delta}(\psi)$. The average power needed to implement the control is defined as the instantaneous power for a single flap averaged over one revolution and multiplied by the number of blades,

$$P_{cs} = \sum_{k=1}^{n_b} \frac{1}{2\pi} \int_0^{2\pi} [-M_\delta(\psi_k)\dot{\delta}(\psi_k)]d\psi_k. \quad (17)$$

It is also important to consider changes in the power required to operate the rotor which may be caused by the ACF. Average rotor power is defined as the instantaneous power required to drive the rotor at a constant angular velocity Ω averaged over one revolution,

$$P_R = \frac{\Omega}{2\pi} \int_0^{2\pi} [-M_{Hz}(\psi)]d\psi, \quad (18)$$

where $M_{Hz}(\psi)$ is the total yawing moment about the hub.

3 AEROELASTIC MODEL FOR BVI ALLEVIATION

3.1 The Structural Dynamic Model

The structural dynamic model adopted has been developed in an earlier study conducted at UCLA [26]. The blade is modeled as an elastic rotating beam that consists of a straight portion and a swept tip, whose orientation with respect to the straight portion is described by a sweep angle Λ_s, positive aft, and an anhedral angle Λ_h, positive up. The blade configuration is shown in Fig. 4. The blade is modeled as a one-dimensional structure composed of a series of beam-type finite elements. A single finite element is used to model the swept tip. The model has provisions for arbitrary cross-sectional shape having multiple cells, generally anisotropic material behavior, transverse shear and out-of-plane warping. The general strain displacement relations for the beam are simplified by using an ordering scheme [24] allowing one to express the strain components in terms of seven unknown variables: the displacement components u,v,w, the elastic twist ϕ, the warping amplitude α, and the transverse shears at the elastic axis $\bar{\gamma}_{x\eta}, \bar{\gamma}_{x\zeta}$. Constitutive relations are introduced based on the assumptions of linear elastic and generally orthotropic material properties.

The aerodynamic loads are calculated from Greenberg's quasisteady aerodynamic theory [27]. The implementation of this aerodynamic model is based on an implicit formulation [28] where the expressions used in the derivation of the aerodynamic loads are

coded in the computer program and assembled numerically during the solution process.

Hamilton's principle is used to formulate the blade dynamic equations. Hermite polynomials are used to discretize the space dependence of the element generalized coordinates: cubic polynomials are used for v and w, quadratic polynomials are used for ϕ, u, α, $\bar{\gamma}_{x\eta}$ and $\bar{\gamma}_{x\zeta}$. The resulting beam element consists of two end nodes and one internal node at its mid-point, and has a total of 23 degrees of freedom, as shown in Fig. 5. Using the interpolation polynomials and carrying out the integration over the element length, the finite element equations of motion for each beam element are written. The nonlinear blade equations of motion are obtained from a finite element assembly procedure:

$$\mathbf{M}(\mathbf{q_b})\,\ddot{\mathbf{q}}_b + \mathbf{C}(\mathbf{q_b},\dot{\mathbf{q}}_b)\,\dot{\mathbf{q}}_b + \mathbf{K}(\mathbf{q_b},\dot{\mathbf{q}}_b,\ddot{\mathbf{q}}_b)\,\mathbf{q}_b +$$
$$\mathbf{F}(\mathbf{q_b},\dot{\mathbf{q}}_b,\ddot{\mathbf{q}}_b) = 0 \quad (19)$$

Subsequently, a modal coordinate transformation is performed to reduce the size of the problem. A substitution approach [26] is used for the treatment of the axial degree of freedom, so as to properly account for the centrifugal force and Coriolis damping effects. In this approach, both the axial degree of freedom and the axial equation of motion are retained in the aeroelastic calculation. Also, an axial mode is included in the modal coordinate transformation.

To be able to model the BVI control problem, an actively controlled trailing edge flap was incorporated in the blade aeroelastic model. The control surface is assumed to be an integral part of the blade, attached by hinges at a number of spanwise locations (Figure 4). The flap is assumed to rotate in the plane of the blade cross section. The flap deflection is considered a controlled quantity. It is also assumed that the presence of the small flap, located in the outboard region of the blade, has a negligible effect on the blade deformation. Thus, only the inertial and aerodynamic effects associated with the flap are included in the aeroelastic model, and the structural effects due to the flap are neglected. Two modules in the original UCLA aeroelastic analysis were modified to account for the presence of the flap, namely: (1) the free vibration analysis, that produces the mode shapes and frequencies, and (2) the aeroelastic response calculation. Additional details on the implementation of the flap in the structural dynamic and aeroelastic analysis can be found in Ref. 14.

3.2 Wake Model

The rotor wake model used in the study has been extracted from the comprehensive rotor analysis code

CAMRAD/JA [29,30] distributed by Johnson Aeronautics. It consists of a wake geometry model, which determines the position of the wake vorticity in space, and a wake calculation model, which calculates the nonuniform induced velocity distribution given the wake geometry.

The wake geometry routine was developed by Scully [31]. The wake vorticity is created in the flow field as the blade rotates, and then convected with the local velocity of the fluid. The local velocity of the fluid consists of the free stream velocity, and the wake self induced velocity. The wake geometry calculation proceeds as follows: (1) the position of the blade generating the wake element is calculated, this is the point at which the wake vorticity is created; (2) the undistorted wake geometry is computed as wake elements are convected downstream from the rotor by the free stream velocity; (3) distortion of wake due to the wake self-induced velocity is computed and added to the undistorted geometry, to obtain a free wake geometry. The position of a generic wake element is identified by its current azimuth position ψ and its age ϕ. Age implies here the nondimensional time that has elapsed between the wake element's current position and the position where it was created. By carrying out this procedure, the position of a generic wake element is written as:

$$\vec{r}_w(\psi, \phi) = \vec{r}_b(\psi - \phi) + \phi \vec{v}_W + \vec{D}(\psi, \phi) \qquad (20)$$

where $\vec{r}_b(\psi - \phi)$ is the position of the blade when it generates the wake element, $\vec{v}_W$ is the free stream velocity, and $\vec{D}(\psi, \phi)$ is the wake distortion, obtained by integrating in time the self induced velocity acting on the wake element. The first term is the position at which the wake was created, the second term is the convection due to the free stream velocity, and the third is the distortion due to the self-induced velocity.

The wake calculation model, developed by Johnson [32], is based on a vortex-lattice approximation for the wake. The wake is composed of two main elements: the tip vortex, which is a strong, concentrated vorticity filament generated at the tip of the blade; and the near wake, an inboard sheet of trailed vorticity, which is much weaker and more diffused than the tip vortex. The tip vortex elements are modeled by line segments with a small viscous core radius, while the inboard wake can be represented by vortex sheet elements or by line segments with a large core radius to eliminate large induced velocities. The near wake vorticity is generally retained for only a number K_{NW} of azimuth steps behind the blade.

The strength of the tip vortex is determined by the bound circulation distribution over the span of the blade by which it is trailed. The selection of a suitable value for the tip vorticity is a delicate issue in wake modeling. Two models are available. The single peak model simply selects the maximum value of the bound circulation over the blade span, Γ_{max}. For helicopters in high speed forward flight a spanwise circulation distribution with two peaks of opposite sign can be encountered. A large positive peak is generally located inboard and a smaller negative peak on the outboard section of blade. The dual peak model is designed for such case. This model identifies the inboard and outboard peaks Γ_I and Γ_O, respectively, and assigns to the tip vortex the circulation value of the outboard peak.

3.3 Combination of the UCLA Structural Dynamic Model with the Wake Module

When implementing the wake model in the UCLA aeroelastic response code, the arrangement of the wake and structural response modules has been modified to be compatible with the special features of the solution procedure. Due to the iterative nature of the wake/structural response coupling procedure, the boundaries between the formulation stage and the solution stage become blurred. Therefore, a detailed description of the solution procedure in the UCLA aeroelastic response calculation is provided so as to clarify the combination of the structural dynamic model with the free wake aerodynamic model.

Two fundamentally different solution procedures are adopted in CAMRAD/JA and in the UCLA aeroelastic model. While the trim/aeroelastic response solution in CAMRAD/JA is sequential and iterative, the one in the UCLA model is simultaneous (i.e. not sequential). These differences required the rearrangement of the various loops into a new arrangement shown in Fig. 6. The coupled trim/aeroelastic analysis in the UCLA code is based on the propulsive trim procedure that has been described earlier in this paper, as given by Eqs. (12) through (16). Additional details on this procedure are given in Ref. 14

4 CONTROL APPROACH

Reduction of the 4/rev hub loads is investigated using a control approach similar to that described in Ref. 4. In this approach, a linear optimal controller is obtained based on the minimization of a performance index J which is a quadratic function of vibration magnitudes z and control input amplitudes u. At the i-th control step,

$$J = z_i^T W_z z_i + u_i^T W_u u_i + \Delta u_i^T W_{\Delta u} \Delta u_i, \qquad (21)$$

where $\Delta u_i = u_i - u_{i-1}$.

In this study, it is assumed that the control input and resulting vibration levels are known without

error. Furthermore, a linear, quasistatic, frequency domain representation of the vibratory response to control is used [3,4], given by

$$z_i = z_{i-1} + T_{i-1}(u_i - u_{i-1}), \qquad (22)$$

where T_{i-1} is a transfer matrix relating vibratory loads to changes in the control input, taken about the current control u_{i-1}:

$$T_{i-1} = \frac{\partial z}{\partial u}\Big|_{u_{i-1}}. \qquad (23)$$

Substituting (22) into (21), and applying the condition

$$\frac{\partial J}{\partial u_i} = 0, \qquad (24)$$

yields the optimal local controller, given by

$$u_i^* = -D_{i-1}^{-1}\{T_{i-1}^T W_z z_{i-1} - W_{\Delta u}u_{i-1} \\ - T_{i-1}^T W_z T_{i-1} u_{i-1}\}, \qquad (25)$$

where

$$D_{i-1} = T_{i-1}^T W_z T_{i-1} + W_u + W_{\Delta u}. \qquad (26)$$

5 RESULTS AND DISCUSSION

5.1 Results for Vibration Alleviation in High Speed Flight

The rotor configuration used in this study is based on the soft-in-plane configuration given in Table 1, with parameters nondimensionalized using the unit quantities

[length]	=	L_b,	length of blade
[mass]	=	M_b,	mass of one blade
[time]	=	$\frac{1}{\Omega}$,	inverse of the rotor speed

These values are given in Table 2 and were chosen to resemble an MBB BO-105 type helicopter [33]. In the results that follow, force and moment have been nondimensionalized by the quantities $M_b\Omega^2 L_b$ and $M_b\Omega^2 L_b^2$, respectively. Unless otherwise indicated, results are presented for a rotor operating in a trimmed condition at an advance ratio of 0.3.

Three control surface configurations, depicted in Fig. 7, have been studied. The first is a servo flap configuration similar to one used in Ref. 4. This is an important test case since it has been extensively studied by Millott and Friedmann [4] using a quasisteady aerodynamic model. In Ref. 10, vibration control studies using the ACF were conducted for the servo flap case using both RFA and modified Theodorsen

aerodynamics. The results generated using RFA aerodynamics have been included in this study for comparison with the other flap configurations.

The size and location of the servo flap was chosen to be identical that used in Ref. 4, and is described in Table 3. The RFA aerodynamic model was based on the optimized configuration presented in Table 4. To account for the 5% higher rotor solidity due to the addition of the servo flap, the weight coefficient C_W was increased by a corresponding amount so that the blade loading, represented by C_W/σ, would remain unchanged.

The second flap configuration considered was a plain flap configuration. In this configuration, the control surface is an integral part of the blade, resulting in a cleaner, low drag implementation when compared to the servo flap. For this reason, it was important to investigate the performance tradeoffs associated with this design and see if there were any significant differences in effectiveness or actuation requirements. The dimensions of the flap are summarized in Table 3. The location and span of the flap are unchanged from the servo flap configuration. However, keeping the flap chord at 25% of the blade chord caused the flap to appear disproportionally large and greatly reduced the space between the (hypothetical) spar and the leading edge of the flap, leaving little room for an actuation mechanism. Instead, the ratio of flap chord to total chord (blade+flap) was kept the same across both configurations. Thus, for the plain flap configuration, the flap chord was decreased from 25% to 20% of the blade chord. Since the addition of a control surface in this configuration does not increase rotor solidity, the weight coefficient was not changed.

The last configuration examined was the dual flap configuration shown in Figure 7. Ideally, two independently controlled flaps spaced widely apart could excite different structural modes and allow more precise control of the structural response. The flap configuration used in this study, given in Table 3, was chosen only to provide an initial assessment of the feasibility of this approach. The best positions and sizes for vibration alleviation were not investigated. The control surfaces were implemented as servo flaps, with the chord and combined length of the flaps the same as for the single servo flap. For this configuration, the aerodynamic model is based on the optimized model given in Table 4, that was modified in Table 5, using the blade segmentation shown in Figure 8.

The objective in this portion of the study was to investigate the effectiveness of the ACF to simultaneously reduce the 4/rev vibratory hub shears and moments due to high speed forward flight and to deter-

mine the associated control power requirements and input amplitudes.

Closed loop control studies utilized the local controller with the control input limited to a combination of 2, 3, 4, and 5/rev harmonics. The control solution typically converged in three or four iterations. For the servo flap and plain flap configurations, the magnitude and rate of the flap inputs were not penalized ($W_u = W_{\Delta u} = 0$). For the dual flap configuration, flap deflection was penalized but flap rate was not. The vibration weighting matrix W_z was assumed to be diagonal and identical for all cases. Although each of the six components of the vibratory response were considered to be of equal importance, the non-dimensionalization scheme reduced the relative magnitude of the hub moments to the hub shears by an order of magnitude. To compensate for this situation, the weighting on the hub moments was scaled by a factor of 10 relative to the weighting on the hub shears.

The first results were generated for the torsionally soft MBB configuration ($\omega_{T1} = 3.17/rev$) described in Table 1. Baseline and controlled 4/rev vibratory loads were obtained using the ACF for the three flap configurations. Some differences in the baseline vibratory loads for the three configurations are due to the differences in blade planform and mass distribution. The plain flap configuration shows the lowest baseline vibration levels of the three configurations over all components of the vibratory response. Compared to the servo flap case, the longitudinal shear is reduced by 2%, the lateral and vertical shears are reduced by more than 4%, and the moments by more than 14%. The dual flap configuration shows an increase in all components of the vibratory response. Rolling and pitching moments show the largest change, with an increase of around 9% over the servo flap levels.

When the controller was engaged, large reductions in the 4/rev vibratory response were obtained, as evident Figure 9. For the servo configuration, each component of the vibratory response is reduced by at least 98%, except longitudinal shear which shows a 96% reduction. There is almost no difference in the effectiveness of the plain flap and the servo flap to control vibration. For the plain flap case, each of the components of the vibratory response was reduced by at least 95%. Of the three configurations, the dual flap is the most effective at reducing the vibratory loads. In this case, each component of the vibratory response was reduced by more than 99.8%. However, these small differences may not have any practical significance.

In Ref. 4, it was shown that the effectiveness of the actively controlled flap to reduce the 4/rev vibratory loads diminishes when the torsional stiffness of the blade is increased. To reexamine this issue, additional results were generated using a higher blade torsional frequency of $\omega_{T1} = 4.5/rev$.

Baseline and controlled vibratory loads found using the stiffer blade are presented in Figure 10. As before, the three flap configurations produce different baseline vibratory responses. Vibratory levels for the plain flap are lower than those found for the servo flap configuration, except for vertical shear which has increased by 10%. The yaw moment is reduced by 7%, and all of the remaining components are within 5% of the servo flap values.

Contrary to the torsionally soft case, the baseline vibration levels for the dual flap configuration are lower than those for the servo flap. The 4/rev vertical shear is more than 16% less, while the hub moments are 5% less. The controlled vibration levels indicate again large reductions in 4/rev loads. However, as in Ref. 4, these reductions are somewhat less than those found for the torsionally softer blade. For the servo flap, longitudinal and lateral shear have been reduced by 88%, while rolling and pitching moment show a 95% reduction which is only slightly less than that found using the softer blade. The effectiveness of the controller in reducing vertical shear is essentially unchanged from the torsionally soft case, reducing it by more than 99%.

The plain flap is less effective than the servo flap in reducing some of the 4/rev components. In particular, longitudinal and lateral shear are reduced by only 84% and 77%, respectively. However, vertical shear and rolling and pitching moments show reductions of more than 96%, and are essentially the same as those achieved using the servo flap.

For the stiffer blade, the dual flap configuration is much more effective than either the single servo or plain flap configurations. Longitudinal and lateral shear were reduced by 98% and 99%, respectively. Vertical shear and rolling and pitching moments were also reduced by more than 99%.

Next, the operational requirements of the ACF for vibration reduction were obtained by generating a complete set of response data over a range of blade torsional frequencies from $2.5/rev \leq \omega_{T1} \leq 4.5/rev$. The flight condition and blade configurations were unchanged from the previous cases.

Figure 11 shows the maximum control deflection required for vibration reduction over the range of blade torsional frequencies. These results show large increases in the control deflections at high blade torsional frequencies. For all configurations, the minimum control deflections were found at the lowest frequencies, between 2.5/rev and 3.0/rev. As evident in Figure 11, much larger control deflections are required

for the plain flap than the servo flap. At lower blade torsional frequencies, the deflection required by the plain flap can be twice that needed by the servo flap. At higher torsional frequencies, the required flap deflections increase significantly for both configurations, reaching almost 19 degrees for the plain flap. The increased control deflections required by the plain flap relative to the servo flap are caused by (a) smaller flap area due to the reduction in flap chord and (b) reduced distance between the flap and the elastic axis of the blade. Both of these changes act to reduce the blade moment produced by a given flap deflection.

For the dual flap configuration, only 1 to 1.5 degrees of control deflection is required for blades with low torsional stiffness. This is approximately half of the deflection required by the single servo flap. At torsional frequencies between 3 and 4/rev, the required deflections for the dual flaps increase and become similar to those required by the single servo flap. At higher torsional frequencies, the required deflections for the dual flaps again become less than those required for the single servo flap.

The average power required to operate the actively controlled flap over one revolution is shown in Figure 12. This value is calculated for the entire rotor (four blades). For all configurations, minimum power occurs for blade torsional frequencies between 2.5 and 3/rev. The average power required for the plain flap is higher than that for the servo flap over the entire range of blade torsional frequencies. The average power requirements for dual flap configuration is greater than that for the servo flap over all but the lowest frequencies (< 3/rev).

To complete the picture of flap operation, Figure 13 illustrates the time history of control deflection for each configuration using the blade with torsional frequency $\omega_{T1} = 3.17$ (MBB type), together with a breakdown of the signal into its harmonic components. As evident in the figure, the largest deflections occur on the retreating side. The plain flap requires the largest peak deflection, and has a response which appears to be an amplified version of the servo flap deflection. Considering the dual flap response, the time history of the inboard and outboard flap deflections are similar. However, a closer examination of the harmonic components reveals some differences. The 3/rev component for the outboard flap is much larger than that for the inboard flap, while the 4/rev component for the outboard flap has virtually disappeared relative to the same component of the inboard flap.

Figure 14 shows the instantaneous power required to drive the flap over one revolution. It has been assumed that the actuator is unable to absorb power from the flap, so negative values of power are set to zero. This Figure shows that the actuator absorbs energy over almost half a revolution. The peak instantaneous power for the plain flap is 53% greater than the peak power required for the servo flap. The peak instantaneous power for the inboard and outboard flaps are 61% and 25% less, respectively, than that for the single servo flap.

Finally, a very interesting side effect of using the ACF for vibration reduction is that it can produce significant changes in *rotor* power requirements. Figure 15 compares rotor power when the flap is fixed and when the flap is being controlled. Using the servo flap, significant decreases in rotor power have been found over the entire range of blade torsional frequencies. Rotor power decreases by more than 2% for blade torsional frequencies between 3 and 3.5/rev. For the plain flap, this decrease can amount to 2.8% of rotor power when the torsional frequency of the blade is around 3.0/rev. As with the single flap case, significant decreases in rotor power are realized when using dual flaps, producing a maximum 3% drop for torsional frequencies around 3/rev, as shown in Figure 15. However, this decrease is limited to torsional frequencies below 4/rev. Above this, rotor power increases, jumping a full 1% at 4.5/rev.

5.2 BVI Alleviation using Active Control

The results presented here are for a straight isotropic hingeless rotor blade, with uniform spanwise properties given in Table 6. The blade is modeled using 5 elements, and the finite element degrees of freedom are reduced, by using 3 flap, 2 lag, 1 torsional and 1 axial modes.

Using the actively controlled flap, simultaneous reduction of 4/rev vibratory hub shears and moments with the nonuniform inflow free wake model was studied. Results were generated for two advance ratios, $\mu = 0.15$ and $\mu = 0.30$. These two cases correspond to two different vibration problems caused by different phenomena. At $\mu = 0.15$ the effects of BVI are strong and represent a major source of higher harmonic airloads, while at $\mu = 0.30$ BVI is less significant and vibratory loads are mostly due to the high forward flight velocity. As indicated previously, the control law for the flap consists of a combination of 2,3,4 and 5/rev harmonic input frequencies. The results from this study are shown in Figures 16 through 27. Figures 16 and 17 show the baseline and controlled vibratory loads. The local controller is effective at reducing the vibratory loads at both advance ratios, but its performance at $\mu = 0.15$ advance ratio is not as good as at $\mu = 0.30$. This is to be expected, since at $\mu = 0.30$ the effects of nonuniform inflow are mild, and earlier results [4] indicated that the actively control flap performed very well when

uniform inflow distribution is assumed. The favorable results obtained for the case of $\mu = 0.15$ indicate that the actively controlled flap is a viable device for alleviating BVI effects at low advance ratios. Figures 18 and 19 illustrate the flap input and its harmonic content for the two cases. The figures emphasize the differences between the flap input at the two advance ratios, indicating that the vibratory loads for the two cases are very different. It should be also noted that for $\mu = 0.15$ considerably larger flap deflections are needed for vibration alleviation.

Figures 20 through 23 show the nondimensional tip deflections in the flap and torsional degrees of freedom. These plots provide insight on the operation of the controller and the mechanism of vibration reduction. From Fig. 21 it is clear that the actively controlled flap does not modify significantly the flapwise dynamics of the blade for the $\mu = 0.30$ case, while it does so at $\mu = 0.15$ as indicated in Fig. 20. This implies that two different strategies are employed by the controller to tackle the vibration alleviation problem at the different advance ratios. At the high advance ratio, $\mu = 0.30$, the normal flapping dynamics of the blade results in a redistribution of the aerodynamic loads over the azimuth. Whereas at $\mu = 0.15$ the controller drives the blade into a region of large flapping dynamics that modifies the relative spacing between the blade and the tip vortices and reduces BVI. These results suggest that the control of BVI induced vibration requires a more refined control strategy where additional variables such as blade-vortex spacing should be included in the objective function. Figures 22 and 23 indicate that blade torsional deflections are also amplified as a result of the controlled flap activity, particularly at the lower advance ratio. This is not surprising since the flap and torsional degrees of freedom have considerable structural coupling.

The large deflection amplitudes induced by the actively controlled flap at $\mu = 0.15$ suggest that higher dynamic loads could be present on the individual blades as a result of the flap activity. Figures 24 through 27 address this issue. The baseline and controlled nondimensional rotating vertical shear and out-of-plane bending moment at the root of the blade for the two advance ratios are compared. The oscillatory amplitudes of the loads in the rotating reference frame increase at $\mu = 0.15$ when compared to $\mu = 0.30$, indicating that the controller alleviates BVI effects at the expense of increased blade loading.

Finally, control power requirements were studied and Figs. 28 and 29 show this comparison. The instantaneous power requirements for the single flap over one revolution are compared with the results from Ref. 10, where a new compressible unsteady

aerodynamic model was used to study vibration reduction using an ACF. In these figures the results denoted by QS Aero - indicate quasisteady Theodorsen type aerodynamics and RFA Aero - indicate the new unsteady aerodynamic model. Note that both cases QS Aero and RFA Aero are combined with uniform inflow. The instantaneous control power is calculated from:

$$P_{cs}(\psi) = -M_\delta(\psi)\,\dot{\delta}(\psi) \qquad (27)$$

where M_δ is the control surface hinge moment and $\dot{\delta}$ is the angular velocity of the control surface about its hinge. Power has been nondimensionalized by dividing it by $m\Omega^3 L_b^3$. As evident from Fig. 28, power requirements at $\mu = 0.30$ are larger for the free wake assumption. Figure 29 compares power requirements at $\mu = 0.15$ with the results shown earlier in Fig. 28. A large increase in power requirement at $\mu = 0.15$ is evident. The instantaneous maximum power for the lower advance ratio is approximately one order of magnitude larger. This is due to the large amplitude of the flap control angles required for BVI-induced vibration reduction. The power requirement distribution at $\mu = 0.15$ exhibits several sharp peaks due to the higher harmonic content of the BVI-induced aerodynamic loads.

6 CONCLUDING REMARKS

Two separate aeroelastic simulation capabilities for modeling vibration reduction in helicopter rotors using partial span, actively controlled, trailing edge flaps have been developed. The first models vibration reduction at high advance ratios ($0.30 < \mu < 0.45$), while the second one focuses on BVI alleviation at low advance ratios. The results represent an important contribution towards understanding the fundamental differences between these two distinct classes of problems and their control using the ACF. The most important conclusions obtained in the course of this research are summarized below.

(1) The ACF is very effective in reducing the 4/rev vibratory hub shears and moments for each of the three flap configurations considered, in high speed flight.

(2) Among the three flap configurations considered, the performance of the plain (or integral) flap was most sensitive to increases in blade torsional stiffness. The servo flap is less sensitive than the plain flap, while the performance of the dual flap configuration was almost completely unaffected by changes in blade torsional stiffness.

(3) There were operational differences between the three configurations considered. The plain flap required greater control deflections and higher control power to achieve the same effectiveness as the other

configurations due to the shorter moment arm between the hinge and the elastic axis of the blade.

(4) The mechanism of vibration reduction using the ACF is fundamentally different for BVI ($\mu = 0.15$) and vibrations due to high speed forward flight ($\mu = 0.30$).

(5) For BVI vibration alleviation the ACF produces reduction of approximately 80%, while in high speed forward flight vibration reduction in excess of 90% is obtained. The magnitude of control angles and the harmonic content are also substantially different between these two cases.

(6) During vibration reduction in presence of BVI the ACF causes large excitations of blade flapwise dynamics, which allow the blade tip to avoid partially the encounter with the vortex. On the other hand when the ACF is used to reduce vibrations due to high speed forward flight, the mechanism of vibration reduction is associated with redistribution of unsteady aerodynamics loading due to the dynamics of the blade.

(7) Alleviation of BVI due to ACF increases the oscillatory bending moments and shears in the rotating system, at the blade root, in the rotating system.

(8) Power requirements for vibration reduction in the presence of BVI are one order of magnitude higher than the ones needed for high speed forward flight, due to the larger magnitude of flap control angles for the $\mu = 0.15$ case.

(9) The ACF displays exceptional potential for alleviating vibratory loads due to BVI, however this problem is more intricate than vibration due to high speed flight. Refined control laws for BVI alleviation should be developed by including the distance between blade tip and vortex in the objective function.

(10) Among the various configurations considered, the dual flap would probably be the most effective for the reduction of vibrations due to high speed forward flight as well as BVI alleviation.

ACKNOWLEDGEMENTS

References

[1] Loewy, R.G., "Helicopter Vibrations, A Technological Perspective," *AHS Journal*, Vol. 29, October 1984, pp. 4-30.

[2] Reichert, G., "Helicopter Vibration Control: A Survey," *Vertica*, Vol. 5, No. 7, 1981, pp. 1-20.

[3] Friedmann, P.P., and Millott, T.A., "Vibration Reduction in Rotorcraft Using Active Control: A Comparison of Various Approaches," *Journal of Guidance, Control, and Dynamics*, Vol. 18, No. 4, July-August 1995, pp. 664-673.

[4] Millott, T.A., and Friedmann, P.P., "Vibration Reduction in Hingeless Rotors using an Actively Controlled Partial Span Trailing Edge Flap Located on the Blade," NASA CR-4611, June 1994.

[5] Straub, F.K., "Active Flap Control for Vibration Reduction and Performance Improvement," Proceedings of the 51st American Helicopter Society Forum, Fort Worth, TX, 1995, pp. 381-392.

[6] Milgram, J., and Chopra, I., "Helicopter Vibration Reduction With Trailing Edge Flaps," AIAA Paper 95-1227-CP, Proceedings of the 36th AIAA/ASME/ASCE/AHS/ASC Structures, Structural Dynamics and Materials Conference, New Orleans, LA, April 10-12, 1995, pp. 601-612.

[7] Leishman, J.G., and Nguyen, K.Q., "A State-Space Representation of Unsteady Aerodynamic Behavior," *AIAA Journal*, Vol. 28, No. 5, May 1990, pp. 836-845.

[8] Leishman, J.G., "Unsteady Lift of a Flapped Airfoil by Indicial Concepts," *Journal of Aircraft*, Vol. 31, No. 2, March-April 1994, pp. 288-297.

[9] Hariharan, N., and Leishman, J.G., "Unsteady Aerodynamics of a Flapped Airfoil in Subsonic Flow by Indicial Concepts," AIAA Paper 95-1228-CP, Proceedings of the 36th AIAA/ASME/ASCE/AHS/ASC Structures, Structural Dynamics and Materials Conference, April 10-12, 1995, New Orleans, LA, pp. 613-634.

[10] Myrtle, T.F., Friedmann, P.P., "New Comprehensive Time Domain Unsteady Aerodynamics for Flapped Airfoils and its Application to Rotor Vibration Reduction Using Active Control," Proceedings of the 53rd Annual Forum of the American Helicopter Society, Virginia Beach, Va, April 29-May 1, 1997.

[11] Myrtle, T.F., Friedmann, P.P., "Vibration Reduction in Rotorcraft Using the Actively Controlled Trailing Edge Flap and Issues Related to Practical Implementation," Proceedings of the 54th Annual Forum of the American Helicopter

Society, Washington D.C., May 20-22, 1998, pp. 602-619.

[12] Myrtle, T.F., "Development of an Improved Aeroelastic Model for the Investigation of Vibration Reduction in Helicopter Rotors Using Trailing Edge Flaps," Ph.D. Dissertation, Mechanical and Aerospace Engineering Dept., University of California, Los Angeles, June 1998.

[13] Fulton, M., and Ormiston, R., "Small-Scale Rotor Experiments with On-Blade Elevons to Reduce Blade Vibratory Loads in Forward Flight," Proc. of the 54th Annual Forum of the American Helicopter Society, Washington, DC, May 20 – 22, 1998, pp. 433 – 451.

[14] deTerlizzi, M. and Friedmann, P. P., "Aeroelastic Response of Swept Tip Rotors Including the Effects of BVI," Proc. of the 54th Annual Forum of the American Helicopter Society, Washington, DC, May 20 – 22, 1998, pp. 644 – 663.

[15] Roger, K.L., "Airplane Math Modeling Methods for Active Control Design," Structural Aspects of Active Controls, AGARD-CP-228, Aug. 1977, pp. 4.1-4.11.

[16] Edwards, J.H., Ashley, H., and Breakwell, J., "Unsteady Aerodynamic Modeling for Arbitrary Motion," *AIAA Journal*, Vol. 17, No. 4, April 1979, pp. 365-374.

[17] Vepa, R., "Finite State Modeling of Aeroelastic Systems," NASA CR-2779, 1977.

[18] Albano, E., and Rodden, W.P., "A Doublet-Lattice Method for Calculating Lift Distributions on Oscillating Surfaces in Subsonic Flows," *AIAA Journal*, Vol. 7, No. 2, February 1969, pp. 279-285.

[19] Possio, C., "L'Azione Aerodinamica sul Profilo Oscillante in un Fluido Compressibile a Velocita Iposonora," *L' Aerotecnica*, t. XVIII, fasc. 4, April 1938. (Also available as British Ministry of Aircraft Production R.T.P translation 987)

[20] van der Wall, B.G., and Leishman, J.G., "On the Influence of Time-Varying Flow Velocity on Unsteady Aerodynamics," *Journal of the American Helicopter Society*, October 1994, pp. 25-36.

[21] Peters, D.A., Barwey, D., "Finite-State Airloads Modeling with Compressibility and Unsteady Freestream,"Proceedings of the Sixth International Workshop on Dynamics and Aeroelastic Stability Modeling of Rotorcraft Systems, Los Angeles, CA, Nov. 8-10, 1995.

[22] Friedmann, P.P., and Hodges, D.H., "Rotary-Wing Aeroelasticity with Application to VTOL Vehicles," *Flight-Vehicle Materials, Structures, and Dynamics- Assessment and Future Direction, Vol. 5, Structural Dynamics and Aeroelasticity*, (Edited by A.K. Noor and S.L. Venneri), published by ASME 1993, Chapter 6, pp. 299-391.

[23] _____, "MACSYMA: Mathematics and System Reference Manual," 15th Edition, 1995.

[24] Friedmann, P.P., "Formulation and Solution of Rotary-Wing Aeroelastic Stability and Response Problems," *Vertica*, Vol. 7, No. 2, 1983, pp. 101-141.

[25] Crespo Da Silva, M.R.M, and Hodges, D.H., "The Role of Computerized Symbolic manipulations in Rotorcraft Dynamic Analysis," *Computer and Mathematics with Application*, Vol. 12A, 1986, pp. 161-172.

[26] Yuan, K. A., and Friedmann, P. P., "Aeroelasticity and Structural Optimization of Composite Helicopter Rotor Blades with Swept Tips." NASA CR 4665, 1995.

[27] Greenberg, J. M., "Airfoil in Sinusoidal Motion in a Pulsating Stream," , NACA TR 1326, 1947.

[28] Celi, R. and Friedmann, P. P., "Rotor Blade Aeroelasticity in Forward Flight with an Implicit Aerodynamic Formulation," *AIAA Journal*, Vol. 26, (12), 1988.

[29] Johnson, W., A Comprehensive Analytical Model of Rotorcraft Aerodynamics and Dynamics, Vol. I: Theory Manual. Johnson Aeronautics, Palo Alto, CA, 1988.

[30] Johnson, W., A Comprehensive Analytical Model of Rotorcraft Aerodynamics and Dynamics, Vol. II: User's Manual. Johnson Aeronautics, Palo Alto, CA 1988.

[31] Scully, M. P., "Computation of Helicopter Rotor Wake Geometry and Its Influence on Rotor Harmonic Airloads". PhD Dissertation, Aeroelastic and Structures Research Laboratory, Massachusetts Institute of Technology, 1975.

[32] Johnson, W., "Wake Model for Helicopter Rotors in High Speed Flight." NASA CR 177507, 1988.

[33] Staley, J.A., "Validation of Rotorcraft Flight Simulation Program Through Correlation with Flight Data for Soft-in-Plane Hingeless Rotors," USAAMRDL-TR-75-50, January 1976.

Table 1: Soft-in-plane elastic blade configuration

Rotor Data	
$n_b = 4$	$L_b = 1.0$
$c_b = 0.05498$	$\theta_{pt} = 0$
$\omega_F = 1.123, 3.41, 7.62$	$C_{do} = 0.01$
$\omega_L = 0.732, 4.46$	
$\omega_{T1} = 3.17$	
$\gamma = 5.5$	$\sigma = 0.07$
Helicopter Data	
$C_W = 0.00515$	$fC_{df} = 0.01 A_R$
$X_{FA} = 0.0$	$Z_{FA} = 0.3$
$X_{FC} = 0.0$	$Z_{FC} = 0.3$

Table 2: Dimensional Parameters (Based on MBB BO-105)

$$L_b = 4.91m$$
$$M_b = 27.35kg$$
$$\Omega = 425RPM$$

Table 3: Flap configuration parameters

$C_f = 0.6$	$X_{Ic} = 0.0$
Servo Flap	
$c_{cs} = c_b/4$	$L_{cs} = 0.12L_b$
$x_{cs} = 0.75L_b$	
Plain Flap	
$c_{cs} = c_b/5$	$L_{cs} = 0.12L_b$
$x_{cs} = 0.75L_b$	
Dual Flap	
$c_{cs1} = c_b/4$	$c_{cs2} = c_b/4$
$L_{cs1} = 0.06L_b$	$L_{cs2} = 0.06L_b$
$x_{cs1} = 0.72L_b$	$x_{cs2} = 0.92L_b$

Table 4: Optimized RFA aerodynamic model

		Aerodynamic Model			
Sec	# Blade Stations	Fitted k range	Lag Terms	# Forces	Aero. States
B	4	0.0-3.0	5	2	40
C	2	0.0-1.1	4	3	24
D	3	0.0-0.9	4	2	24
				Total:	88

Table 5: RFA aerodynamic model for the dual flap configuration

		Aerodynamic Model			
Sec	# Blade Stations	Fitted k range	Lag Terms	# Forces	Aero. States
B	4	0.0-3.0	5	2	40
C	1	0.0-1.1	4	3	12
D	2	0.0-1.1	4	2	16
E	1	0.0-1.1	4	3	12
F	1	0.0-0.9	4	2	8
				Total:	88

Table 6: Soft-in-plane Isotropic Rotor Blade Data

Rotor Data	
$EI_y/m\Omega^2 R^4 = 0.0106$	
$EI_z/m\Omega^2 R^4 = 0.0301$	
$GJ/m\Omega^2 R^4 = 0.001473$	
$L_b = 1.0$	$n_b = 4$
$(k_A/k_m)^2 = 2.0415$	$a = 2\pi$
$k_{m1}/R = 0.0$	$k_{m2}/R = 0.02$
$\gamma = 5.5$	$\beta_p = 0.0$
$\sigma = 0.07$	$c_b/R = 0.055$
Helicopter Data	
$C_W = 0.00515$	$C_{d0} = 0.01$
$Z_{FC}/R = 0.50$	$Z_{FA}/R = 0.25$
$X_{FC}/R = 0.0$	$X_{FA}/R = 0.0$
Flap Data	
$L_{cs} = 0.12L_b$	$c_{cs} = c_b/4$
$x_{cs} = 0.75L_b$	

Figure 1: Fully elastic blade model incorporating a partial span trailing edge flap.
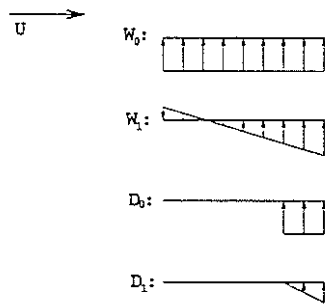
Figure 2: Normal velocity distributions corresponding to generalized airfoil and flap motions W_0, W_1, D_0, and D_1.
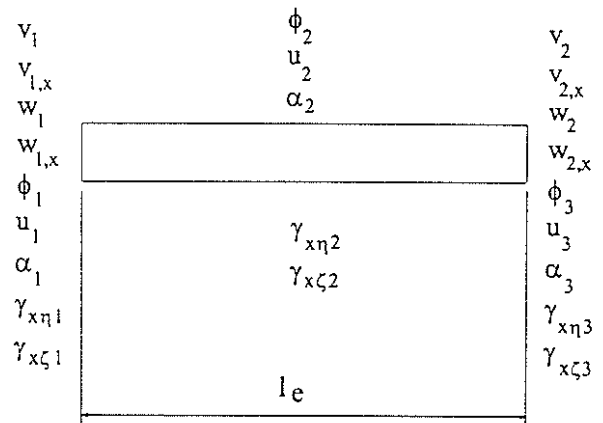
Figure 5: Finite element degrees of freedom.
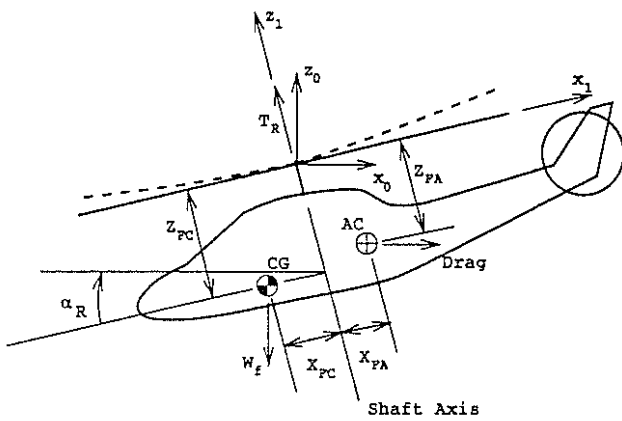
Figure 3: Schematic of a helicopter in level forward flight.
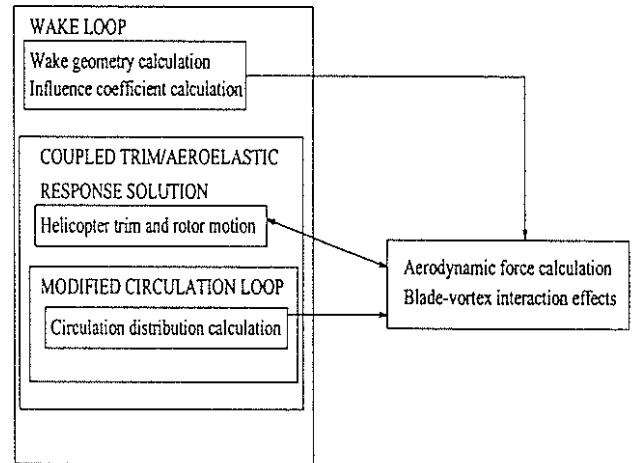
Figure 6: UCLA model: solution structure
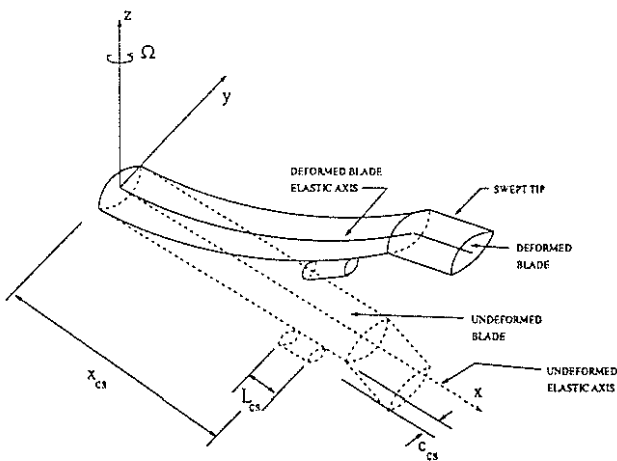
Figure 4: Schematic model of swept tip hingeless blade with actively controlled partial span trailing edge flap.
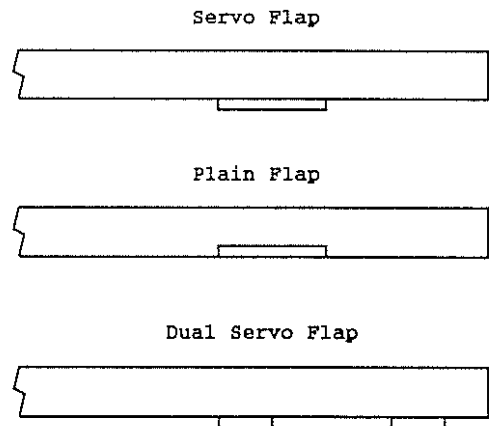
Figure 7: Three control surface configurations investigated in this study.
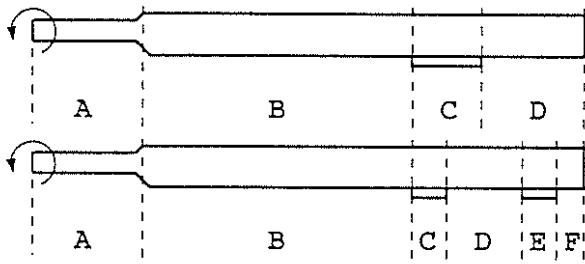
Figure 8: Blade segments for single and dual flap configurations.
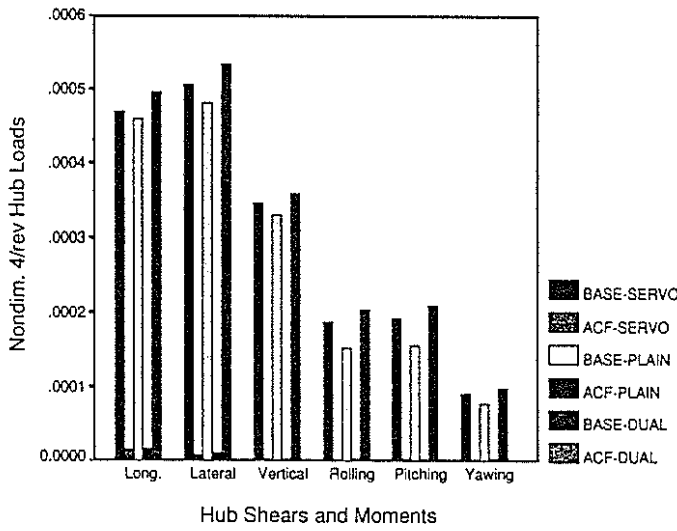
Figure 9: Baseline and controlled values of the 4/rev hub shears and moments, $\mu = 0.3$, $\omega_{T1} = 3.17/rev$.
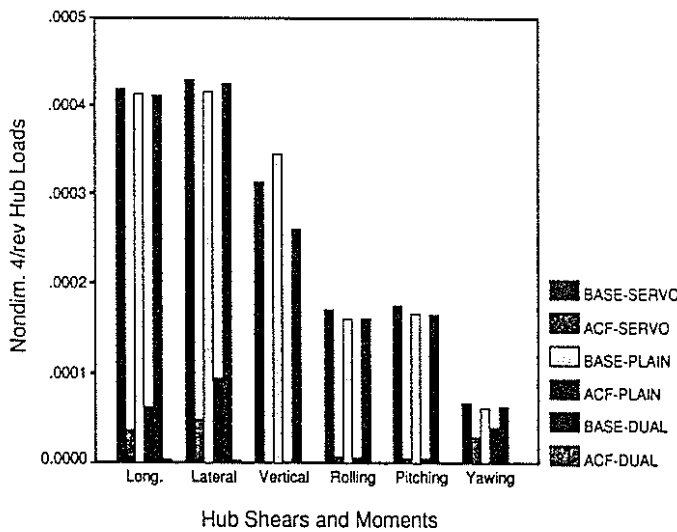
Figure 10: Baseline and controlled values of the 4/rev hub shears and moments, $\mu = 0.3$, $\omega_{T1} = 4.5/rev$.
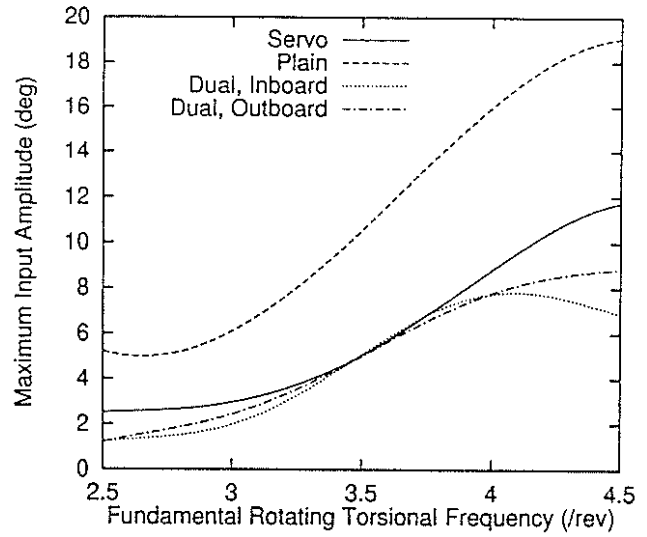
Figure 11: Maximum flap deflection over a range of blade torsional frequencies, $\mu = 0.3$.
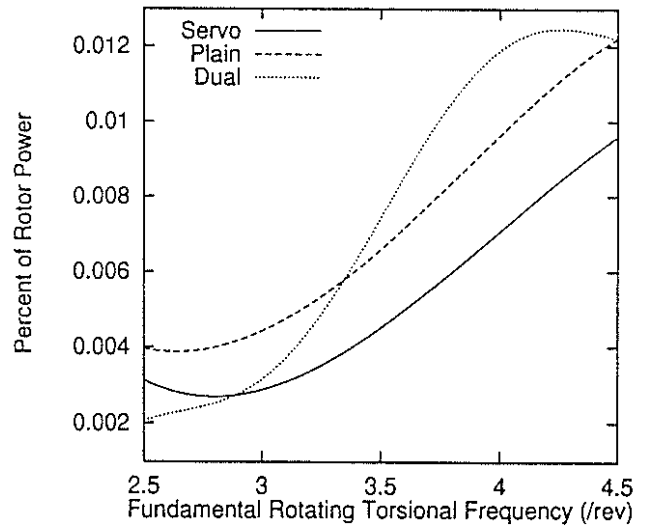
Figure 12: Control power for vibration reduction as a percentage of total rotor power, measured over a range of blade torsional frequencies, $\mu = 0.3$.

Figure 14: Instantaneous control power requirements over one revolution, $\mu = 0.3$.
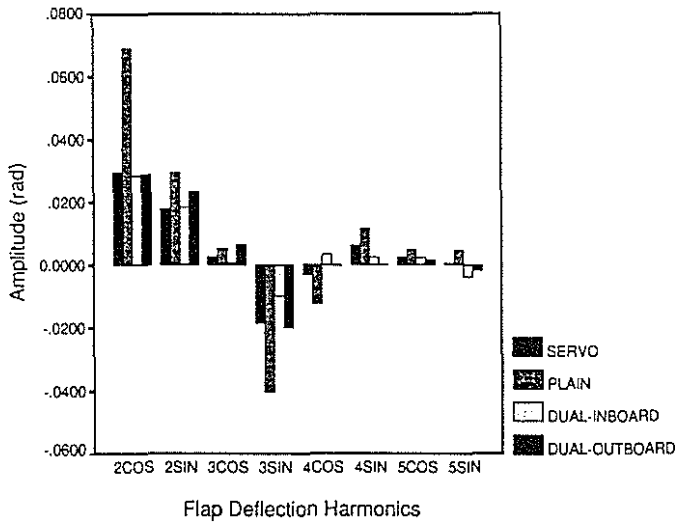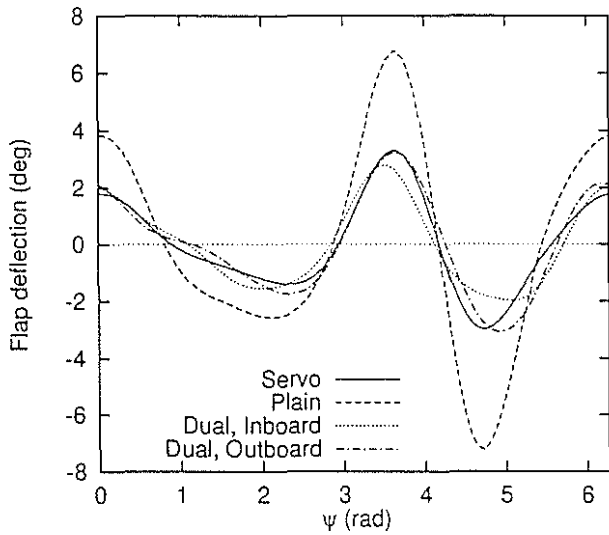
Figure 13: (a) Flap deflection, (b) Flap deflection harmonic components, $\mu = 0.3$, $\omega_{T1} = 3.17/rev$.
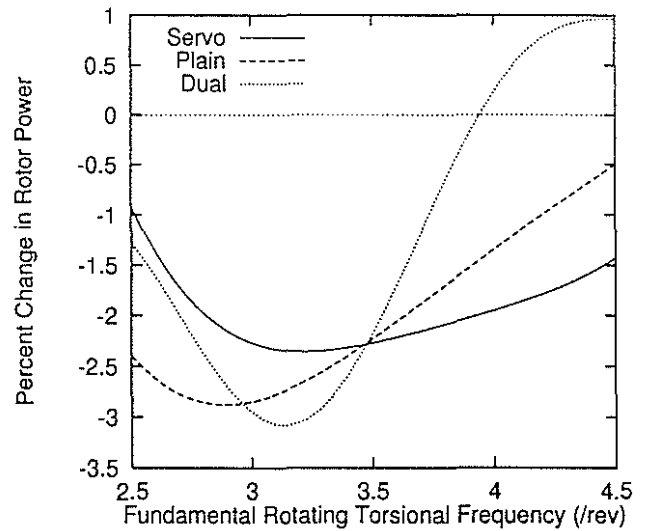
Figure 15: Percent change in rotor power requirements with control for vibration reduction, measured over a range of blade torsional frequencies, $\mu = 0.3$.
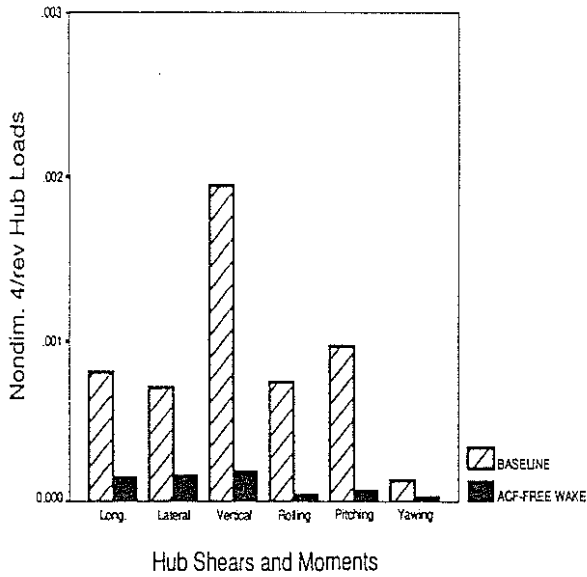
Figure 16: Simultaneous reduction of the 4/rev hub shears and moments, $\mu = 0.15$.
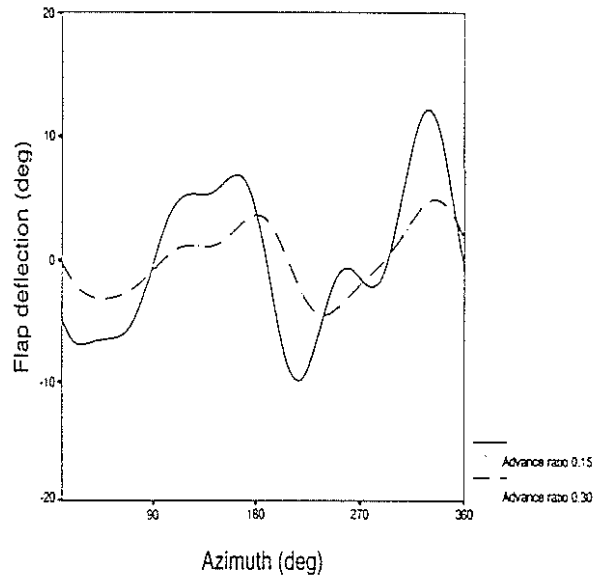
Figure 18: Flap deflection history at the advance ratios $\mu = 0.15$ and $\mu = 0.30$.
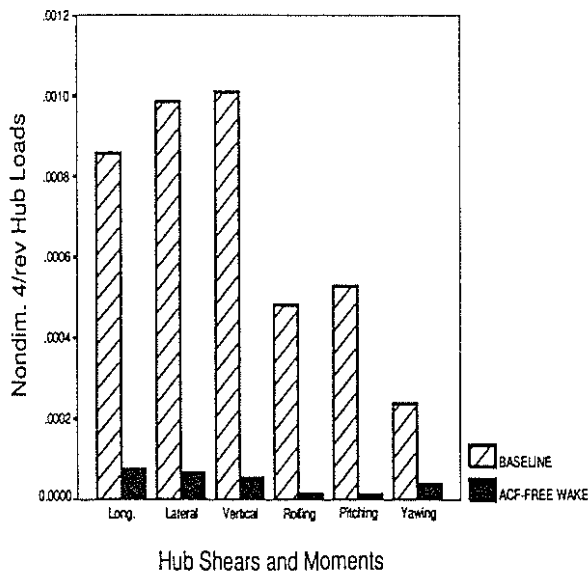
Figure 17: Simultaneous reduction of the 4/rev hub shears and moments, $\mu = 0.30$.
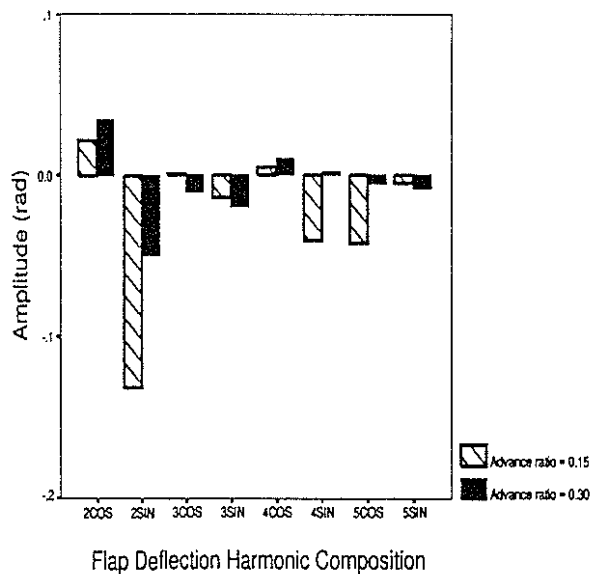
Figure 19: Flap deflection harmonic components at the advance ratios $\mu = 0.15$ and $\mu = 0.30$.
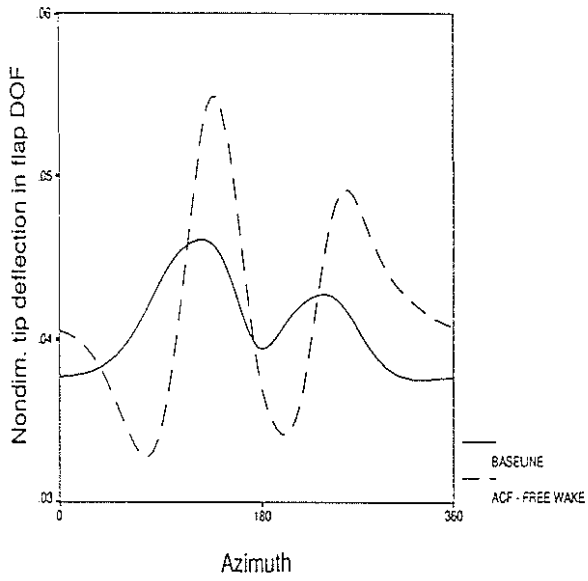
Figure 20: Nondimensional tip deflections in flap degree of freedom, $\mu = 0.15$.
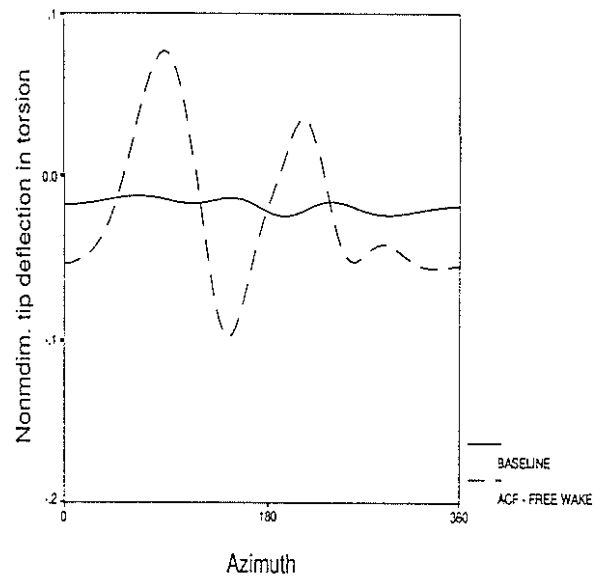
Figure 22: Nondimensional tip deflections in torsional degree of freedom, $\mu = 0.15$.
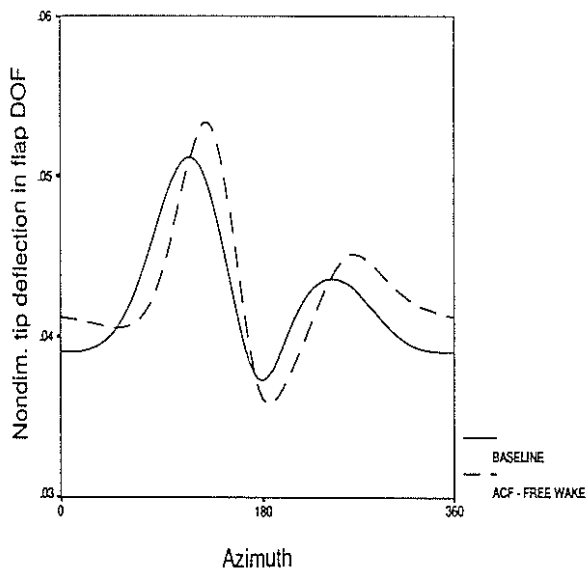
Figure 21: Nondimensional tip deflections in flap degree of freedom, $\mu = 0.30$.
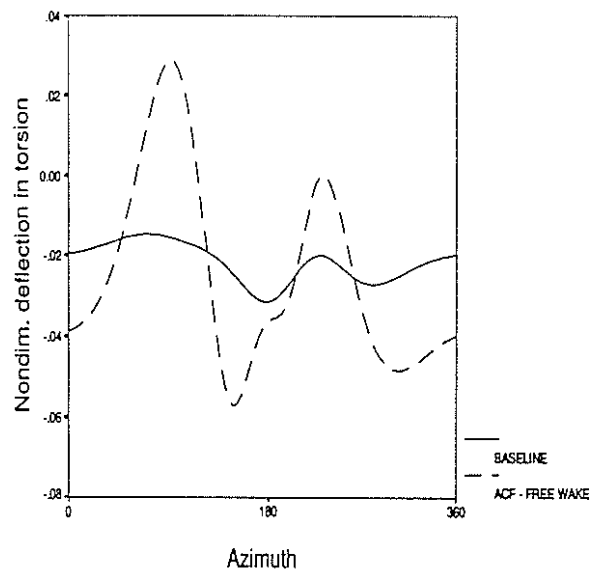
Figure 23: Nondimensional tip deflections in torsional degree of freedom, $\mu = 0.30$.
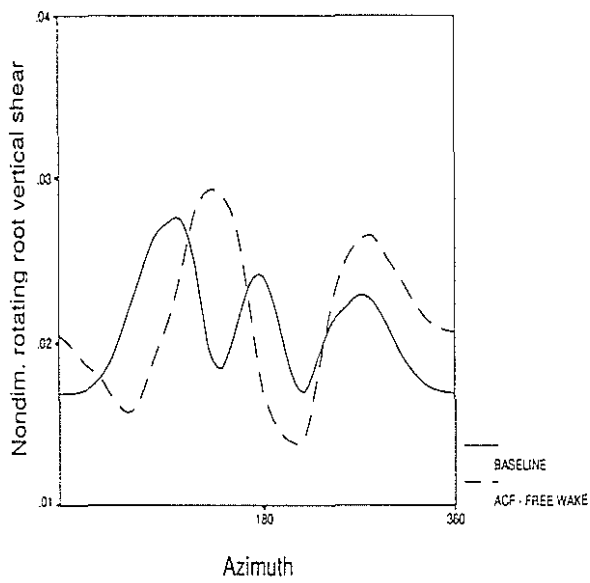
Figure 24: Nondimensional rotating root vertical shear, $\mu = 0.15$.
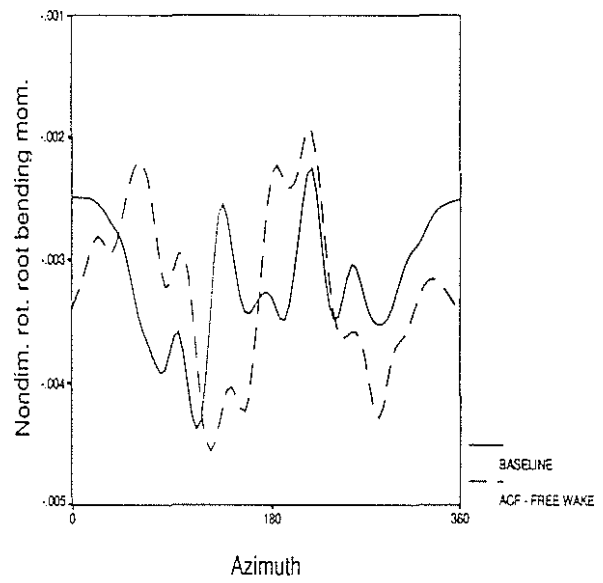
Figure 26: Nondimensional rotating out-of-plane root bending moment, $\mu = 0.15$.
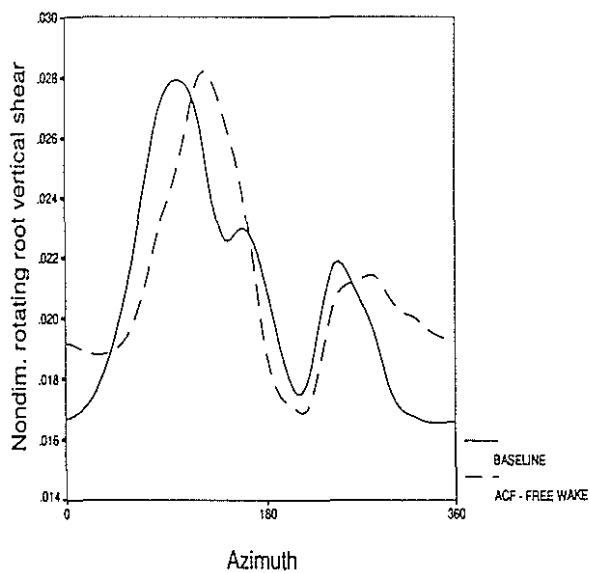
Figure 25: Nondimensional rotating root vertical shear, $\mu = 0.30$.
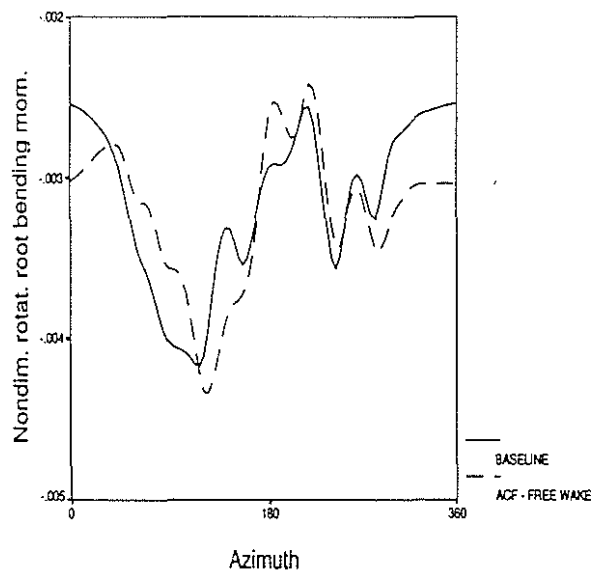
Figure 27: Nondimensional rotating out-of-plane root bending moment, $\mu = 0.30$.
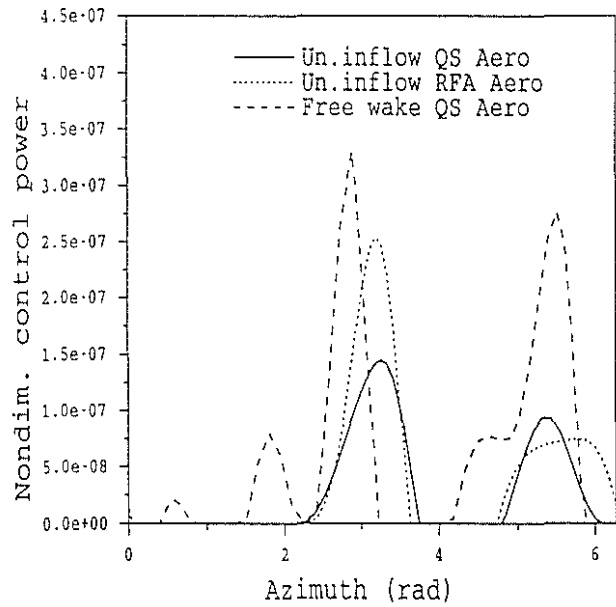
Figure 28: Control power requirements over one revolution, $\mu = 0.30$.
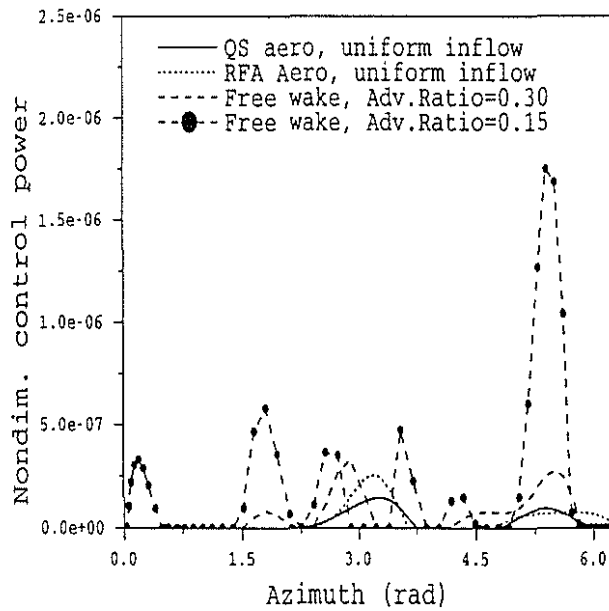
Figure 29: Control power requirements over one revolution, $\mu = 0.15$ and $\mu = 0.30$